Photoacoustic tomography of monkey brain using virtual point ultrasonic transducers

Liming Nie
Zijian Guo
Lihong V. Wang

Photoacoustic tomography of monkey brain using virtual point ultrasonic transducers

Liming Nie, Zijian Guo, and Lihong V. Wang
Washington University in St. Louis, Department of Biomedical Engineering, Optical Imaging Laboratory, One
Brookings Drive, Campus Box 1097, St. Louis, Missouri 63130

Abstract. A photoacoustic tomography system (PAT) using virtual point ultrasonic transducers was developed and applied to image a monkey brain. The custom-built transducers provide a 10-fold greater field-of-view (FOV) than finite-aperture unfocused transducers as well as an improved signal-to-noise ratio (SNR) and reduced artifacts rather than negative-lens transducers. Their tangential resolution, radial resolution, and (SNR) improvements were quantified using tissue phantoms. Our PAT system can achieve high uniformity in both resolution (<1 mm) and SNR (>8) within a large FOV of 6 cm in diameter, even when the imaging objects are enclosed by a monkey skull. The cerebral cortex of a monkey brain was accurately mapped transcranially, through a skull ranging from 2 to 4 mm in thickness. This study demonstrates that PAT can overcome the optical and ultrasound attenuation of a relatively thick skull and can potentially be applied to human neonatal brain imaging. © *2011 Society of Photo-Optical Instrumentation Engineers (SPIE)*. [DOI: 10.1117/1.3595842]

Keywords: photoacoustic tomography; human neonatal brain; monkey brain; virtual point ultrasonic detectors.

Paper 10674RR received Dec. 22, 2010; revised manuscript received Apr. 8, 2011; accepted for publication May 9, 2011; published online Jul. 1, 2011.

1 Introduction

Photoacoustic tomography (PAT) is a noninvasive and nonionizing hybrid imaging technique that combines strong optical absorption contrast and high ultrasound spatial resolution.[1,2] It relies on the thermoelastic effect for generating acoustic pressure waves under thermal and stress confinement conditions. A laser pulse is used to irradiate tissue, causing optical absorption, rapid thermoelastic expansion, and then acoustic pressure generation.[3,4] When the excitation laser is replaced by microwave sources, the technique is named thermoacoustic tomography (TAT),[5] PAT has already demonstrated its ability in high-quality *in vivo* vascular structural imaging and hemodynamic functional imaging.[6–8] In this article, we report large field of view (FOV) PAT using virtual point ultrasonic detectors for monkey brain imaging.

Structural and functional imaging of the mouse brain has been well demonstrated with PAT.[6,7] However, since traditional flat transducers can provide only a small FOV with acceptable sensitivity, PAT and TAT of the cerebral cortex in large animals[9,10] is challenging. There is always a tradeoff between the sensitivity and the detecting angle: large-aperture detectors can achieve better sensitivity while compromising the FOV, whereas small point detectors produce a larger FOV while compromising the detection sensitivity. We previously proposed a method of attaching a negative lens to a flat transducer to overcome the aforementioned problem,[11,12] and the spatial resolution was preserved in a large FOV. However, the negative lens introduced reflection, attenuation, and reverberations of ultrasonic waves, and thus the sensitivity and the reconstruction accuracy decreased. As a consequence, the negative-lens

transducers were designed primarily for conceptual demonstration, and are not suitable for robust and accurate animal imaging. The negative lens ultrasonic transducer is one variant of virtual point detectors. In this study, two other types of virtual point ultrasonic detectors were custom built through the use of concave and convex transducer surfaces without attached lenses. In comparison to the negative-lens ultrasonic transducers that we studied previously,[11] the custom-built detectors retain a large acceptance angle, provide a higher S signal-to-noise ratio (SNR) (~15% improvement), and avoid ultrasound reverberations. As a result, the shapes of the imaging targets far away from the scanning center were preserved with both uniform high spatial resolution and SNR. This salient feature allowed us to successfully accomplish PAT of a monkey brain cortex, where more blood vessels were observed with higher contrast and resolution in comparison to our previous work.[9]

Ultrasound imaging is an established pediatric brain imaging method used before the closure of the fontanelles. After the closure of the fontanelles, the image quality degrades, due to severe distortion and attenuation of ultrasound waves in phase and amplitude by the skull.[13] In contrast to ultrasound imaging, PAT detects ultrasound signals through one-way propagation, and thus suffers much less distortion and attenuation by the skull. In addition, PAT based on endogenous hemoglobin contrast is particularly suitable for imaging blood vessels of the cerebral cortex. Multiwavelength PAT can be used to compute oxygen saturation of hemoglobin and thus to monitor functional activities of the human cerebral cortex.

2 Methods and Materials

A PAT system was designed for monkey brain imaging, as shown in Fig. 1(a). Light from a tunable dye laser (NS, Sirah), pumped

---

Address all correspondence to: Lihong V. Wang, Washington University in St. Louis, Biomedical, Engineering, One Brookings Drive, Campus Box, 1097, St. Louis, Missouri 63130. Tel: (314) 935–6152; Fax: (314) 935–7448; E-mail: lhwang@biomed.wustl.edu.
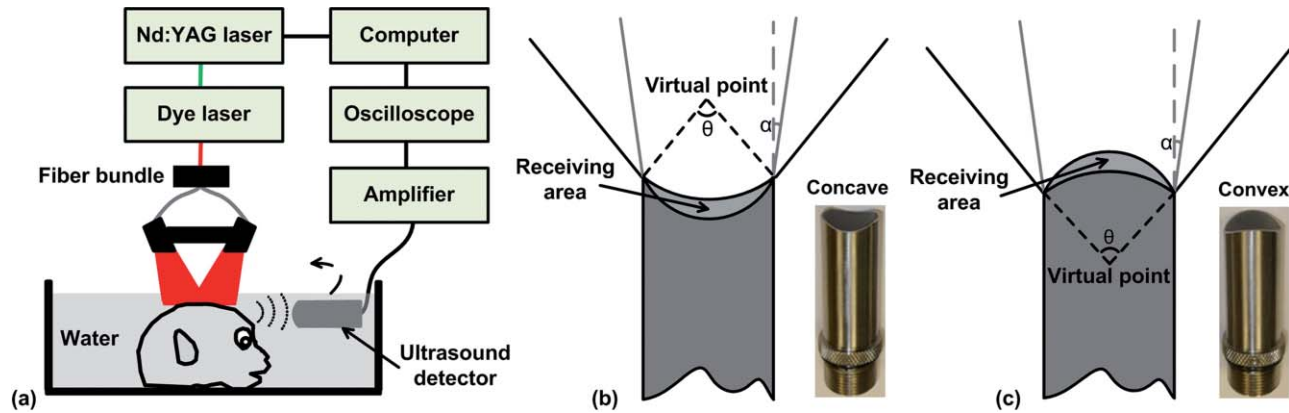
Fig. 1 Schematic of the PAT system and virtual point detectors. (a) The schematic of the PAT system. Illustration of the signal acceptance modes of the (b) concave and (c) convex virtual point detector with their photographs. The gray solid lines represent the acceptance angle of the flat transducer, and the black solid lines represent the acceptance angle of the concave and convex virtual point detectors.

by a Q-switched Nd:YAG laser (PRO-350–10, Newport) with a 6.5-ns pulse duration and a 10-Hz pulse repetition rate, was coupled to a multimode fiber bundle (CB18043, Fiberguide). The laser irradiation area could be adjusted by tuning the distance between the fiber bundle and the imaging target. The optical wavelength was tunable between 606 and 678 nm. Unless otherwise noted, PAT images were acquired at 630 nm, and the incident laser fluence on the target surface was ~8 mJ/cm^2, well within the American National Standards Institute's limits.[14] A personal computer (PC) provided a synchronized clock signal to trigger the laser and oscilloscope simultaneously. The target sample was immersed in water and irradiated by a laser beam from the top, and an ultrasound detector scanned the sample circularly with a scanning radius of 10 cm on the plane orthogonal to the irradiation direction over 200 angles. The photoacoustic (PA) signals were detected by the ultrasound transducer, and were amplified by a 50-dB amplifier (5072 PR, Panametrics, Waltham, Massachusetts) and directed to a digital oscilloscope (TDS5054, Tektronix, Beaverton, Oregon), then sent to the PC for subsequent image processing.

The custom-built virtual point ultrasonic detectors (from GE Healthcare) had a 2.25-MHz central frequency with 70% bandwidth. They were categorized as concave and convex virtual point detectors according to their surface geometric shapes, as shown in Figs. 1(b) and 1(c). The concave and convex virtual point detectors are also referred to as positively and negatively focused transducers, respectively. These two virtual detectors are equivalent to point detectors in their receiving angle and FOV; however, they possess a much greater receiving surface and sensitivity. Specifically, the virtual point of the concave transducer is located in front of the receiving surface, while the virtual point of the convex transducer is located behind the receiving surface. The cylindrically focused transducers are focused in the scanning plane but unfocused in the elevation direction. For the concave transducer, the focus is 9.7 mm in front of the deepest point on the transducer surface; for the convex transducer, the focus is 9.7 mm behind the most protruding point on the transducer surface. The acceptance angle is defined as the angle at which the radiation power decreases more than 6 dB. The convex and concave parts of the curved surfaces are 2.5 mm in depth and their cross sectional diameters are 13 mm. Thus, their receiving

angles are 87.8 deg, compared to 8.6 deg for a flat transducer.[15] Flat and negative-lens transducers were used for comparison. The flat transducer (ISS 2.25 × 0.5 COM, Krautkramer, GE Healthcare) has similar parameters to the virtual point detectors, except for its flat receiving surface. The negative-lens transducer was made by gluing a negative cylindrical lens onto the active surface of the flat transducer.[12]

A back-projection algorithm was employed to reconstruct an image.[6] In the image reconstruction of the virtual point detectors, we adjusted the signal time delay to accommodate the spatial
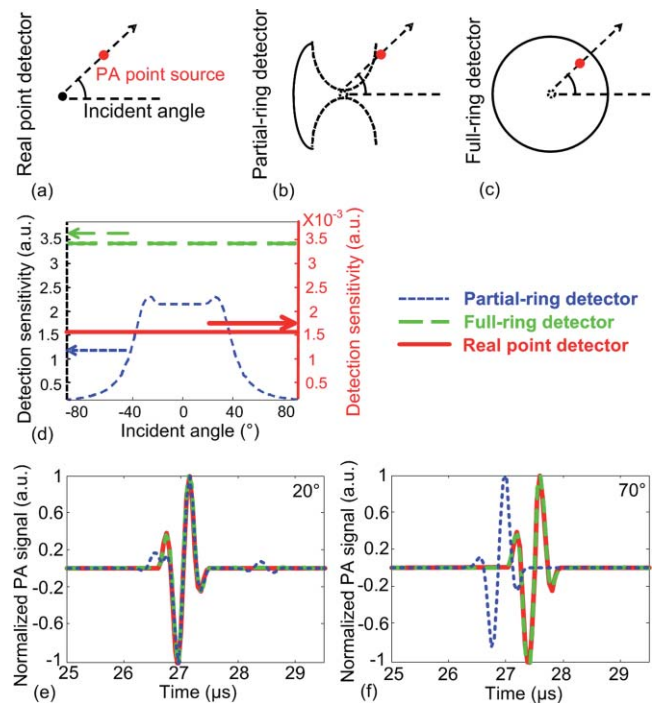
Fig. 2 Comparison of a real point detector, a partial-ring detector, and a full-ring detector. Schematics of the PA signal detection mode of (a) a real point detector, (b) a partial-ring detector, and (c) a full-ring detector. (d) Detection sensitivity distributions versus incident angle for the three detectors. Normalized PA signals from the point source acquired with the three detectors at the (e) 20 deg incident angle and (f) 70 deg incident angle.
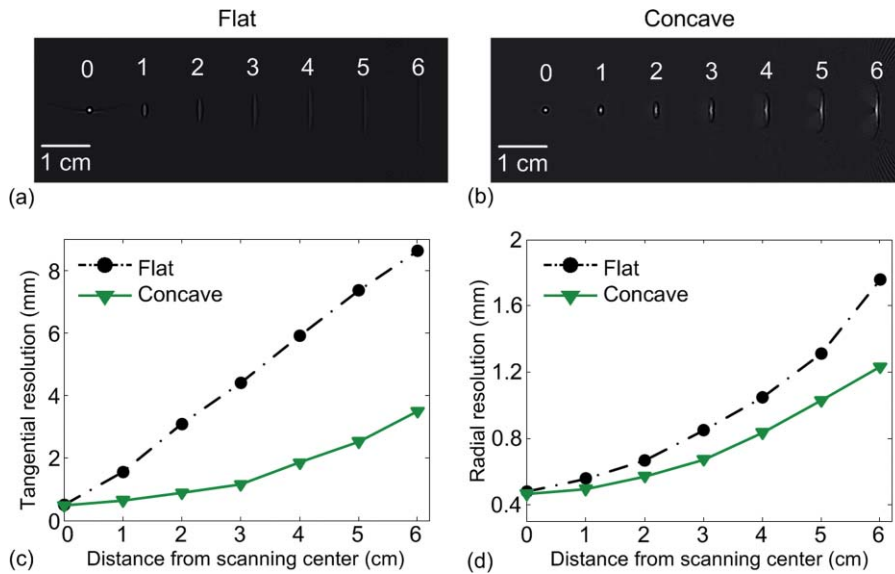
Fig. 3 Simulation results of the resolutions versus distance from the scanning center. Reconstructed PAT image of seven point targets acquired with (a) the flat transducer, and (b) the concave virtual point detector. (c) Tangential resolution and (d) radial resolution versus distance from the scanning center.

difference between the locations of the virtual point and the transducer's active surface.

We first used the FIELD II software package[15] to simulate and compare a real point ultrasonic transducer, a partial-ring ultrasonic transducer used in the experiments, and a full-ring ultrasonic transducer (Fig. 2). The simulation parameters are set to be the same as in the experiments (2.25-MHz central frequency) and the simulated PA point sources are located 50 mm away from the virtual point. The tangential and radial resolutions versus the distance from the scanning center for a flat transducer and a concave virtual point detector were also simulated and compared (Fig. 3).

To experimentally quantify the tangential resolution, radial resolution, and SNR improvements, we imaged seven identical needles with diameters of 0.5 mm. The needles were inserted into a piece of agar in a line 1 cm apart, as shown in Fig. 4(a). Five identical transparent plastic tubes with an inner diameter of 7 mm were filled with bovine blood and placed in different positions, as shown in Fig. 5(a), for PAT imaging at 610 nm light wavelength.

A head of a 4-month-old rhesus monkey, immediately immersed in 10% formalin solution after harvest, was obtained from the Wisconsin National Primate Research Center. The blood vasculature was well maintained for PAT experiments, and the hair and scalp were removed. The dimensions of the head in the axial view were about 8 cm × 6 cm, and the laser irradiation area was about 5 cm × 5 cm. The skull thickness was inhomogeneous, ranging from 2 to 4 mm (Fig. 6).

3 Results

In the simulation study, the signal receiving schematic of a real point ultrasonic transducer, a partial-ring ultrasonic transducer, and a full-ring ultrasonic transducer are shown in Figs. 2(a)–2(c), respectively. Figure 2(d) shows the detection sensitivity versus the incident angle relative to the axial direction.
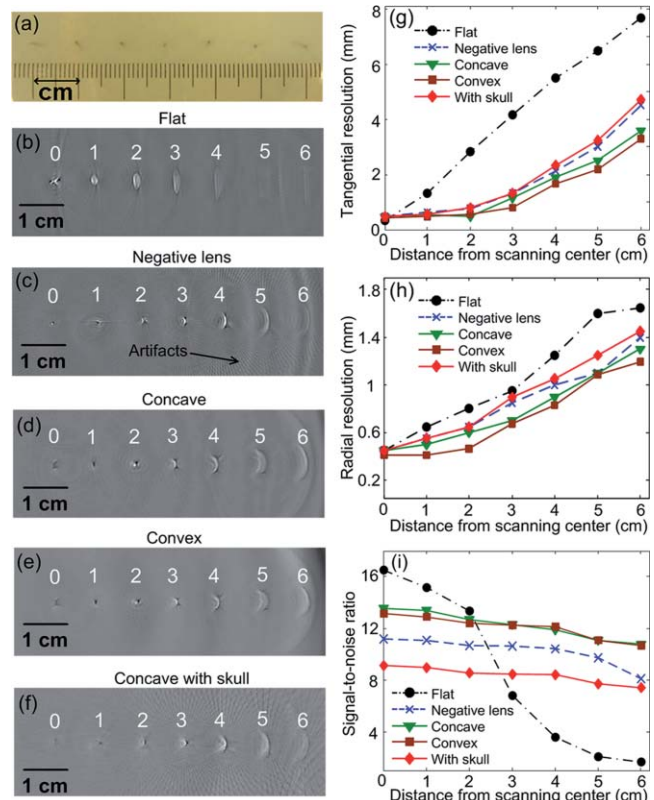
Fig. 4 PAT of needles and the resolution and SNR quantifications. (a) Photograph of seven needles inserted in agar at different distances from the scanning center. PAT of the phantom acquired with (b) a flat transducer, (c) a negative-lens transducer, (d) a concave virtual point transducer, (e) a convex virtual point transducer, and (f) a virtual point detector with the phantom enclosed by a monkey skull. Quantification of (g) tangential resolution, (h) radial resolution, and (i) SNR of the PAT systems versus distance from the scanning center.
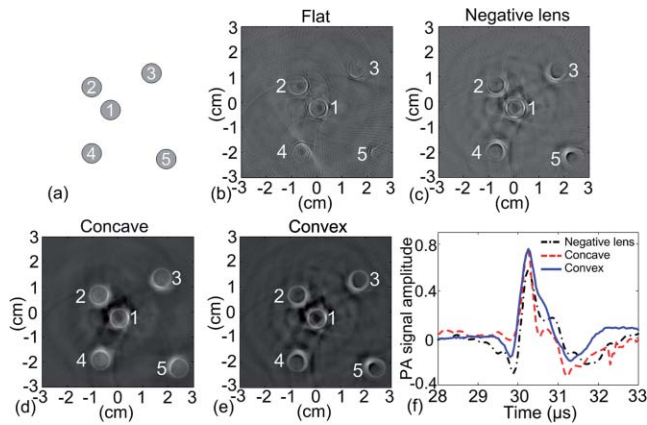
Fig. 5 PAT of bovine blood in tubes. (a) Schematic of the five tubes' placement. PAT images acquired by (b) a flat transducer, (c) a negative lens transducer, (d) a concave virtual point transducer, and (e) convex virtual point transducer. (f) Comparison of the detectors' sensitivities.

Fig. 6 PAT of monkey brain cortex. PAT of monkey brain (a) with cranium and dura mater intact acquired by a flat transducer, (b) with cranium and dura mater intact acquired by a virtual point detector, and (c) without cranium and dura mater acquired by a virtual point detector. (d) Photograph of the exposed monkey brain after removing the cranium and dura mater.

Since the partial-ring detector has a limited full acceptance angle (~87.8 deg), the sensitivity decreases when the PA source is located outside the FOV of the partial-ring detector. On the other hand, the partial-ring detector and the full-ring detector have orders of magnitude with higher sensitivity than the real point detector, because they have much larger detecting surfaces. The sensitivity is defined as the maximum pressure received from the field point. We separately simulated the three detector responses to the point PA source located along two incident angles (20 and 70 deg), shown in Figs. 2(e) and 2(f). As shown in Fig. 2(f), when the PA point source is located outside the full acceptance angle (70 deg > 87.8 deg/2), detection artifacts appear. However, the partial-ring detectors used in our experiments can be approximated as real point detectors when the point source is located within the acceptance angle [Fig. 2(e)]. Figures 3(a) and 3(b) show the reconstructed images of seven simulated point targets acquired with the flat transducer and the concave virtual point detector, respectively. The tangential and radial resolutions are quantified by calculating the full width at half maximum (FWHM) of the main lobe of the point spread function in the corresponding directions, as shown in Figs. 3(c) and 3(d). For the flat transducer, the tangential and radial resolutions deteriorate by ~13 and ~3 fold, respectively, over a 6 cm range. By contrast, the virtual point detector shows significant improvement in both the tangential and radial resolutions (<1 mm) within a large FOV of 6 cm in diameter because of its larger acceptance angle.

Figures 4(b)–4(e) show the PAT images of needles acquired experimentally with the flat, negative-lens, concave, and convex transducers. Compared to the image acquired with the flat transducer [Fig. 4(b)], the image acquired with the virtual point detectors [Figs. 4(d) and 4(e)] show significant improvements in tangential resolution, radial resolution, and SNR. We observe greater than 3-fold tangential resolution enhancement when the object is 2 cm away from the scanning center and greater than 3-fold SNR enhancement when the object is 4 cm away from the scanning center. The further the distance from the scanning center, the greater the improvement gained. In particular, needles 5 and 6 at distances of 5 and 6 cm from the scanning center are almost invisible in Fig. 4(b), because the acceptance angle of the flat transducer is limited and the two needles were out

of the imaging FOV. Compared to the image acquired with the negative-lens transducer [Fig. 4(c)], the image acquired with the virtual point detectors [Figs. 4(d) and 4(e)] show less artifacts and an improved SNR (~15% improvement).

To investigate the effect of a monkey skull on SNR and resolutions, we also acquired a PAT image of the needle phantoms enclosed by a monkey skull ranging from 2 to 4 mm in thickness with the concave virtual point detector as shown in Fig. 4(f). SNR and resolution decreased in the reconstructed image; however, the needles are still distinguishable [Fig. 4(f)]. The tangential resolution, radial resolution, and SNR versus the distance from the scanning center are quantified in Figs. 4(g)–4(i). Even when the imaging objects are enclosed by a monkey skull, our PAT system with virtual point detectors can achieve a relatively uniform high resolution (<1 mm) and high SNR (>8) within a large FOV of 6 cm in diameter, and thus it is suitable for a monkey brain or human neonatal brain imaging.

Figures 5(b) and 5(e) show PAT images of five tubes filled with bovine blood, acquired with the flat transducer, negative lens transducer, concave virtual point detector, and convex virtual point detector, respectively. Images of the tubes far from the scanning center (3, 4, and 5) are distorted, as shown in Figs. 5(b) and 5(c), but well preserved as shown in Figs. 5(d) and 5(e). In addition, compared to the images acquired with the negative lens transducer [Fig. 5(c)], the images acquired with the virtual point detectors [Figs. 5(d) and 5(e)] have ~15% sensitivity enhancement as shown in Fig. 5(f).

Figure 6 shows PAT of monkey brain images acquired (a) by the flat transducer with the cranium and dura mater intact, and (b) by the convex virtual point detector with and (c)

without the cranium and dura mater, respectively. Images similar to those shown in Figs. 6(b) and 6(c) were obtained by the concave virtual point detector. We can associate blood vessels by labeling them with the same numbers in Figs. 6(a)–6(d). Compared to Figs. 6(b) and 6(c), Fig. 6(a) shows only the blood vessels in the scanning center, and blood vessels 4, 5, 7, 8, 9, 12, and 13 disappear because of the limited detection angle of the flat transducer. Vascular structures can be clearly identified through the intact skull from the PAT image in Fig. 6(b). The blood vessels in Fig. 6(c) show increased contrast over those in Fig. 6(b), which is attributable to optical and ultrasound attenuation in the cranium and dura mater. The mean FWHM diameter of the reconstructed blood vessels was then quantified, with and without cranium, to be 0.73 and 0.45 mm, respectively. A photograph of the exposed brain cortex of the rhesus monkey is shown in Fig. 6(d).

4 Conclusions

In summary, we developed and applied virtual point detectors for the PAT of the monkey brain. Compared to flat ultrasonic transducers, virtual point ultrasonic transducers greatly improve the tangential resolution, radial resolution, and SNR at the periphery. The increase in the acceptance angle of the detectors enabled us to image a larger FOV, and thus the object shapes in the reconstructed images were well preserved, even when the target was far from the scanning center. Compared to the negative-lens ultrasonic transducers,[12] the virtual point ultrasonic detectors provide an improved SNR (∼15% improvement) and avoid reverberation artifacts in the reconstructed images. Our experimental results also show that PAT can overcome the effect of a relatively thick skull bone to a great extent, and that the PAT brain cortex imaging of large animals is feasible. Therefore, PAT may be potentially used for monitoring the blood-related pathological and physiological status of human brains, especially for neonatal brains before the closure of fontanelles.

References

1. H. F. Zhang, K. Maslov, G. Stoica, and L. V. Wang, "Functional photoacoustic microscopy for high-resolution and noninvasive *in vivo* imaging," *Nat. Biotech.* **24**(7), 848–851 (2006).
2. D. Razansky, C. Vinegoni, and V. Ntziachristos, "Multispectral photoacoustic imaging of fluorochromes in small animals," *Opt. Lett.* **32**, 2891–2893 (2007).
3. J. G. Laufer, D. T. Delpy, C. E. Elwell, and P. C. Beard, "Quantitative spatially resolved measurement of tissue chromophore concentrations using photoacoustic spectroscopy: application to the measurement of blood oxygenation and haemoglobin concentration," *Phys. Med. Biol.* **52**, 141–168 (2007).
4. V. P. Zharov, E. I. Galanzha, E. V. Shashkov, N. G. Khlebtsov, and V. V. Tuchin, "In vivo photoacoustic flow cytometry for monitoring of circulating single cancer cells and contrast agents," *Opt. Lett.* **31**, 3623–3625 (2006).
5. L. V. Wang, X. Zhao, H. Sun, and G. Ku, ''Microwave-induced acoustic imaging of biological tissues,'' *Rev. Sci. Instrum.* **70**, 3744–3748 (1999).
6. X. Wang, Y. Pang, G. Ku, X. Xie, G. Stoica, and L. V. Wang, "Noninvasive laser-induced photoacoustic tomography for structural and functional *in vivo* imaging of the brain," *Nat. Biotechnol.* **21**(7), 803–806 (2003).
7. S. Yang, D. Xing, Q. Zhou, L. Xiang, and Y. Lao, "Functional imaging of cerebrovascular activities in small animals using high-resolution photoacoustic tomography," *Med. Phys.* **34**, 3294–3301 (2007).
8. H. P. Brecht, R. Su, M. Fronheiser, S. A. Ermilov, A. Conjusteau, and A. A. Oraevsky, "Whole-body three dimensional optoacoustic tomography system for small animals," *J. Biomed. Opt.* **14**(6), 064007 (2009).
9. X. M. Yang and L. V. Wang, "Monkey brain cortex imaging by photoacoustic tomography," *J. Biomed. Opt.* **13**(4), 044009 (2008).
10. Y. Xu and L. H. V. Wang, "Rhesus monkey brain imaging through intact skull with thermoacoustic tomography," *IEEE Trans. Ultrason. Ferroelect. Freq. Contr.* **53**, 542–548 (2006).
11. C. H. Li, G. Ku, and L. V. Wang, "Negative lens concept for photoacoustic tomography," *Phys. Rev. E* **78**(2), 021901 (2008).
12. M. Pramanik, G. Ku, and L. V. Wang, "Tangential resolution improvement in thermoacoustic and photoacoustic tomography using a negative acoustic lens," *J. Biomed. Opt.* **14**(2), 024028 (2009).
13. S. W. Smith, K. Chu, S. F. Idriss, N. M. Ivancevich, E. D. Light, and P. D. Wolf, "Feasibility study: Real-time 3D ultrasound imaging of the brain," *Ultrasound Med. Biol.* **30**(10), 1365–1371 (2004).
14. Laser Institute of America, "American national standard for safe use of lasers," *ANSI Z136*.1–2000, American National Standards Institute, New York (2000).
15. J. A. Jensen and N. B. Svendsen, "Calculation of pressure fields from arbitrarily shaped, apodized, and excited ultrasound transducers," *IEEE Trans. Ultrason.Ferroelec. Freq. Contr.* **39**, 262–267 (1992).